INSTITUTE OF PHYSICS PUBLISHING JOURNAL OF PHYSICS D: APPLIED PHYSICS

J. Phys. D: Appl. Phys. **36** (2003) 1388–1398 PII: S0022-3727(03)59453-0

Heat transfer and fluid flow during laser spot welding of 304 stainless steel

X He[1], P W Fuerschbach[2] and T DebRoy[1]

[1] Department of Materials Science and Engineering, The Pennsylvania State University, USA
[2] Joining and Coating Department, Sandia National Laboratories, USA

Received 11 February 2003
Published 28 May 2003
Online at stacks.iop.org/JPhysD/36/1388

Abstract

The evolution of temperature and velocity fields during laser spot welding of 304 stainless steel was studied using a transient, heat transfer and fluid flow model based on the solution of the equations of conservation of mass, momentum and energy in the weld pool. The weld pool geometry, weld thermal cycles and various solidification parameters were calculated. The fusion zone geometry, calculated from the transient heat transfer and fluid flow model, was in good agreement with the corresponding experimentally measured values for various welding conditions. Dimensional analysis was used to understand the importance of heat transfer by conduction and convection and the roles of various driving forces for convection in the weld pool. During solidification, the mushy zone grew at a rapid rate and the maximum size of the mushy zone was reached when the pure liquid region vanished. The solidification rate of the mushy zone/liquid interface was shown to increase while the temperature gradient in the liquid zone at this interface decreased as solidification of the weld pool progressed. The heating and cooling rates, temperature gradient and the solidification rate at the mushy zone/liquid interface for laser spot welding were much higher than those for the moving and spot gas tungsten arc welding.

1. Introduction

Pulse Nd : YAG spot welds are widely used for assembly and closure of high reliability electrical and electronic packages for the telecommunications, defence, aerospace, and medical industries. Laser spot welding has an important advantage for these applications because it can deliver a minimum amount of energy to very small components with high precision. Laser spot welds behave very differently from their moving weld counterparts because the temperature profiles never reach a steady state and the heating and cooling rates for these welds are much higher than those of linear welds. Laser spot welds are characterized by small weld pool size, rapid changes of temperature and very short duration of the process. These characteristics make physical measurements of important parameters such as temperature and velocity fields, solidification rate and thermal cycles during laser spot welding very difficult. These parameters are important because the weld pool convection patterns and the heating and cooling rates determine the geometry, composition, structure and the resulting properties of the spot welds.

In recent decades, numerical calculations of heat transfer and fluid flow have been utilized to understand the evolution of temperature and velocity fields, and weld geometry that cannot be obtained otherwise. However, most of these studies were concerned with arc welds where the timescale is of the order of several seconds. The timescale is much shorter for laser spot welding. The heat transfer and fluid flow during laser spot welding still remain to be investigated to understand how the velocity and temperature fields evolve during heating and cooling and how the mushy zone region behaves. Such a computationally intensive investigation, requiring use of fine grids and very small time steps has now become practical because of recent advances in the computational hardware and software.

Several models have been developed to predict the temperature and velocity fields in the weld pool during laser welding. Cline and Anthony [1] studied the effects of laser spot size, velocity and power level on the temperature distribution, cooling rate and depth of melting of 304 stainless steel. However, the convection in the weld pool was not considered in the model. Mazumder and Steen [2] developed a numerical

model of the continuous laser welding process considering heat conduction. The finite difference technique was used. Frewin and Scott [3] used a finite element model of the heat flow during pulsed laser beam welding. The transient temperature profiles and the dimensions of fusion zone and HAZ were calculated. Katayama and Mizutani [4] developed a heat conduction and solidification model considering the effects of microsegregation and latent heat. Recently, Chang and Na [5] applied the finite element method and neural network to study laser spot welding of 304 stainless steel. This combined model could be effectively applied for the prediction of bead shapes of laser spot welding. In summary, transport phenomena based numerical models have been successful in revealing special features in transient spot welding processes such as the transient nature of the solidification rate [6, 7].

A numerical model to simulate heat transfer and fluid flow during steady and transient fusion welding has been developed and refined during the past 20 years at Penn State. The model has been used to calculate weld pool geometry, temperature and velocity fields during welding of pure iron [8, 9], stainless steel [10–13], low alloy steel [14, 15], aluminium alloy [16] and titanium alloy [17] under different welding conditions. Calculations were done for both moving and stationary heat sources and for laser beam as well as arc welding. The computed temperature fields were useful for the calculation of vaporization rates of alloying elements [8–11, 16], weld metal microstructure [9, 15], inclusion characteristics [14], grain growth [17], phase transformation kinetics [18] and concentrations of dissolved gases in the weld metal [19, 20].

In this study, a transient numerical model was used to understand heat transfer and fluid flow during laser spot welding of 304 stainless steel. Surface tension and buoyancy forces were considered for the calculation of transient weld pool convection. Very fine grids and small time steps were used to achieve accuracy in the calculations. The calculated weld pool dimensions were compared with the corresponding measured values to validate the model. Dimensional analysis was carried out to understand the significance of the various driving forces for the liquid pool convection. The behaviour of the mushy zone, i.e. the solid–liquid two phase region, during heating and cooling was investigated. Results also revealed information about the important solidification parameters R, the solidification rate, and G, the temperature gradient in the liquid at the mushy zone/liquid front as a function of time. These data are useful for determining the solidification morphology and the scale of the solidification substructure. This work demonstrates that the application of numerical transport phenomena can significantly add to the quantitative knowledge base in fusion welding.

2. Experimental procedure

Multiple 304 stainless steel pulse Nd : YAG laser spot welds were produced at Sandia National Laboratories. The steel had the following composition: 1 wt% Mn, 18.1 wt% Cr, 8.6 wt% Ni, 0.012 wt% P, 0.003 wt% S, and balance Fe. A Raytheon SS 525 laser was used for laser spot welding with pulse energies between 2.1 and 5.9 J, and pulse durations of 3.0 and 4.0 ms. For each combination of energy and duration, the laser beam was defocused to different extents to obtain various spot diameters and power densities. By controlling the beam shutter, individual spot welds from the pulsed laser beam were made on $3 \times 10 \times 17\,\text{mm}^3$ EDM wire cut samples. Up to 15 individual spot welds were made on each of the samples. Laser spot size was measured with $50\,\mu$m Kapton film using the method described elsewhere [21]. Supplementary argon shielding of plate surface during welding was provided to reduce oxide formation and for protection of the lens. Longitudinal metallographic cross-section measurements through several collinear welds for each plate were averaged to determine weld pool width and depth. The experimental conditions are indicated in table 1.

Table 1. The experimental conditions.

Material	304 stainless steel
Pulse energy	2.1, 3.2, 5.9 J
Pulse power	0.53, 1.0, 1.9 kW
Pulse duration	3.0, 4.0 ms
Spot radius	0.159–0.57 mm
Spot welds	15 per plate
Shielding gas	Argon

3. Mathematical formulation

3.1. Governing equations

Because of the axisymmetric nature of spot welding [6, 12, 22], the governing equations can be solved in a two-dimensional system to calculate the temperature and velocity fields. However, since the heat transfer and fluid flow model is also used for the calculations of welding with a moving heat source which is a three-dimensional problem, the same transient, three-dimensional, heat transfer and fluid flow model was used for the laser spot welding. An incompressible, laminar and Newtonian liquid flow is assumed in the weld pool. The following equations were solved with appropriate boundary conditions.

Mass conservation:

$$\nabla \cdot (V) = 0 \tag{1}$$

Momentum conservation:

$$\rho \frac{\partial (V)}{\partial t} = -\rho \nabla \cdot (VV) + \nabla \cdot (\mu \nabla V) - \nabla P + S_1 \tag{2}$$

where ρ is the density, t is the time, V is the velocity, P is the pressure, μ is the viscosity and S_1 is the source terms in momentum equation which is expressed as:

$$S_1 = S_{\text{diff}} - C \frac{(1 - f_{\text{L}})^2}{f_{\text{L}}^3 + B} V + \rho g \beta (T - T_{\text{ref}}) \tag{3}$$

where S_{diff} is a source term representing viscous diffusion which originates from writing the momentum equations in a general form [23]. For the x-component of the momentum equation, the source term S_{diff} can be expressed as:

$$S_{\text{diff}\,x} = \frac{\partial}{\partial x}\left(\mu \frac{\partial V_x}{\partial x}\right) + \frac{\partial}{\partial y}\left(\mu \frac{\partial V_y}{\partial x}\right) + \frac{\partial}{\partial z}\left(\mu \frac{\partial V_z}{\partial x}\right) \tag{4}$$

The second term in the right-hand side in equation (3) represents the frictional dissipation of momentum in the mushy

zone according to the Carman-Kozeny equation for flow through porous media [24, 25], f_L is the liquid fraction, B is a very small positive number introduced to avoid division by zero, C represents mushy zone morphology and is usually a large number to force the velocity in the solid zone to be zero, β is the thermal expansion coefficient of the liquid, T is the temperature, and T_{ref} is the reference temperature.

Energy conservation:

$$\frac{\partial(\rho h)}{\partial t} = -\nabla \cdot (\rho V h) + \nabla \cdot \left(\frac{k}{C_p} \nabla h \right) + S_2 \tag{5}$$

where h is the sensible heat, k is the thermal conductivity, C_p is the specific heat and S_2 is the source term in energy equation which is expressed as:

$$S_2 = -\rho \frac{\partial \Delta H}{\partial t} - \rho \nabla \cdot (V \Delta H) \tag{6}$$

where ΔH is the latent heat.

3.2. Boundary conditions

A three-dimensional Cartesian coordinate system is used in the calculation, while only half of the workpiece is considered since the weld is symmetrical about the weld centreline. The input heat on the top surface is assumed to have Gaussian distribution and given as [26]:

$$H_{in} = \frac{f Q \eta}{r_b^2} \exp\left(-\frac{f(x^2 + y^2)}{r_b^2} \right) \tag{7}$$

where f is the heat distribution factor, Q is the laser power, η is the absorption coefficient, r_b is the beam radius. For laser welding, distribution factor f is taken as 3.0 [27]. Laser power and beam radius were experimentally measured. The reported values of the absorption coefficient vary significantly [28–31]. For example, Cremers *et al* [28] indicated absorption coefficient of Nd : YAG laser in 316 stainless steel in the range of 0.21–0.62. The absorption coefficient has been related to the substrate resistivity and the wavelength of the laser radiation by the following relation [31]:

$$\eta(T) = 0.365 \left(\frac{\alpha}{\lambda} \right)^{1/2} - 0.0667 \left(\frac{\alpha}{\lambda} \right) + 0.006 \left(\frac{\alpha}{\lambda} \right)^{3/2} \tag{8}$$

where λ is the wavelength, α is the electrical resistivity of the materials. The average electrical resistivity of 304 stainless steel is 80 $\mu\Omega$ cm [32], and the wavelength of Nd : YAG laser is 1.064 μm. Substituting these values into equation (8), the absorption coefficient is obtained as 0.27, which is the value taken in the calculations reported in this paper.

The temperature and velocity boundary conditions used in the calculations are the same as those used in the GTA spot welding. These conditions are fairly straightforward and they have been explicitly defined in a recent paper [33].

3.3. Discretization of governing equations

The governing equations were discretized using the control volume method, where a whole rectangular computational domain was divided into small rectangular control volumes. A scalar grid point was located at the centre of each control volume, storing the values for scalar variables such as pressure and enthalpy. In order to ensure the stability of numerical calculation, velocity components were arranged on different grid points, staggered with respect to scalar grid points. In another word, velocity components were calculated for the points that lie on the faces of the control volumes. Thus, the control volumes for scalars were different from those for the vectors. Discretized equations for a variable were formulated by integrating the corresponding governing equation over the three-dimensional control volumes. The final discretized equation takes the following form [23]:

$$a_P \phi_P = a_E \phi_E + a_W \phi_W + a_N \phi_N + a_S \phi_S + a_T \phi_T + a_B \phi_B + a_P^0 \phi_P^0 + S_U \Delta V \tag{9}$$

where subscript P represents a given grid point, while subscripts E, W, N, S, T, B represent the east, west, north, south, top and bottom neighbours of the given grid point P, respectively. The symbol ϕ represents a dependant variable such as velocity or enthalpy, a is the coefficient calculated based on the power law scheme, ΔV is the volume of the control volume, a_P^0 and ϕ_P^0 are the coefficient and value of the dependant variable at the previous time step, respectively. S_U is the constant part of the source term S, which can be expressed as:

$$S = S_U + S_P \phi_P \tag{10}$$

The coefficient a_P is defined as:

$$a_P = a_E + a_W + a_N + a_S + a_T + a_B + a_P^0 + S_P \Delta V \tag{11}$$

The governing equations were then solved iteratively on a line-by-line basis using a tri-diagonal matrix algorithm (TDMA). The detailed procedure to solve the equations is described in [23].

3.4. Grid spacings and time steps

A very fine grid system and small time step were used to improve the computation accuracy. A typical grid system used in this paper contained 83 × 45 × 60 grid points, and the corresponding computational domain had dimensions of 30 mm in length, 15 mm in width and 15 mm in depth. Spatially non-uniform grids were used for maximum resolution of variables. A finer grid spacing was used near the heat source. The minimum grid space along the x, y and z directions were about 17 μm, 17 μm and 10 μm, respectively. The time step used in the heating part was 0.05 ms, while the time step for the cooling part was 0.005 ms to obtain more accurate results.

3.5. Convergence criteria

In this model, two convergence criteria are used, i.e. residuals and heat balance. The residuals for velocities and enthalpy are defined as:

$$R = \left\{ \sum_{\text{domain}} |(a_E \phi_E + a_W \phi_W + a_N \phi_N + a_S \phi_S + a_T \phi_T + a_B \phi_B + a_P^0 \phi_P^0 + S_U \Delta V)/a_P - \phi_P| \right\} \left\{ \sum_{\text{domain}} |\phi_P| \right\}^{-1} \tag{12}$$

Table 2. Data used for calculations [21, 32, 34–36].

Property/parameter	Value
Density of liquid metal (gm cm^{-3})	7.2
Absorption coefficient	0.27
Effective viscosity (gm cm^{-1} s^{-1})	1
Solidus temperature (K)	1697
Liquidus temperature (K)	1727
Enthalpy of solid at melting point (cal gm^{-1})	286.6
Enthalpy of liquid at melting point (cal gm^{-1})	300.0
Specific heat of solid (cal gm^{-1} K^{-1})	0.17
Specific heat of liquid (cal gm^{-1} K^{-1})	0.20
Thermal conductivity of solid (cal cm^{-1} s^{-1} K^{-1})	0.046
Effective thermal conductivity of liquid (cal cm^{-1} s^{-1} K^{-1})	0.5
Temperature coefficient of surface tension (dynes cm^{-1} K^{-1})	−0.43
Coefficient of thermal expansion	1.96e−5

Convergence was assumed when the value of R in equation (12) reached $\leqslant 10^{-4}$. In addition, the following heat balance criterion for the convergence of the computed temperature profiles was also checked.

$$\theta = \left| \frac{\text{net heat input}}{\text{total heat output} + \text{heat accumulation}} \right| \qquad (13)$$

Upon convergence, heat balance ratio θ should be very close to 1. In this study, the convergence criterion used was $0.999 \leqslant \theta \leqslant 1.001$. The data used for calculations [21, 32, 34–36] are presented in table 2.

4. Results and discussion

4.1. Comparison between the calculated and experimental results

The experimentally determined weld pool cross sections are compared with the corresponding computed values in figure 1. It is observed that the calculated weld pool geometry and dimensions agree well with the experimental results. Both the experimental and the computed results show that with the increase in the beam diameter, the weld pool becomes wider and shallower. This observation is consistent with distribution of energy over a wider area with the increase in the beam diameter. Since the temperature coefficient of surface tension is negative, the molten metal on the surface flows from the centre to the periphery of the pool. As a result, the convection in the weld pool aids in the transport of heat from the middle to the periphery of the weld pool. The role of convection in the heat transfer will be discussed in more details later in this paper. The experimental values of weld pool depth and width for various laser power densities agreed well with the corresponding calculated values as shown in figure 2. The fair agreement indicates validity of the transient heat transfer and fluid flow model.

4.2. Temperature and velocity fields

Figures 3(*a*)–(*e*) show the computed temperature and velocity fields as a function of time. The contour values in the figures represent temperatures in kelvin. In the initial period, the weld pool expands rapidly in size and the temperatures and

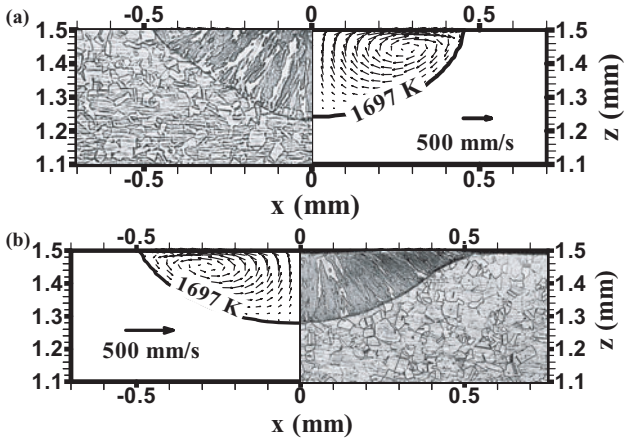

Figure 1. Experimental and calculated weld pool cross sections for laser power of 1967 W and pulse duration of 3 ms. (*a*) Beam radius: 0.428 mm; (*b*) beam radius: 0.57 mm.

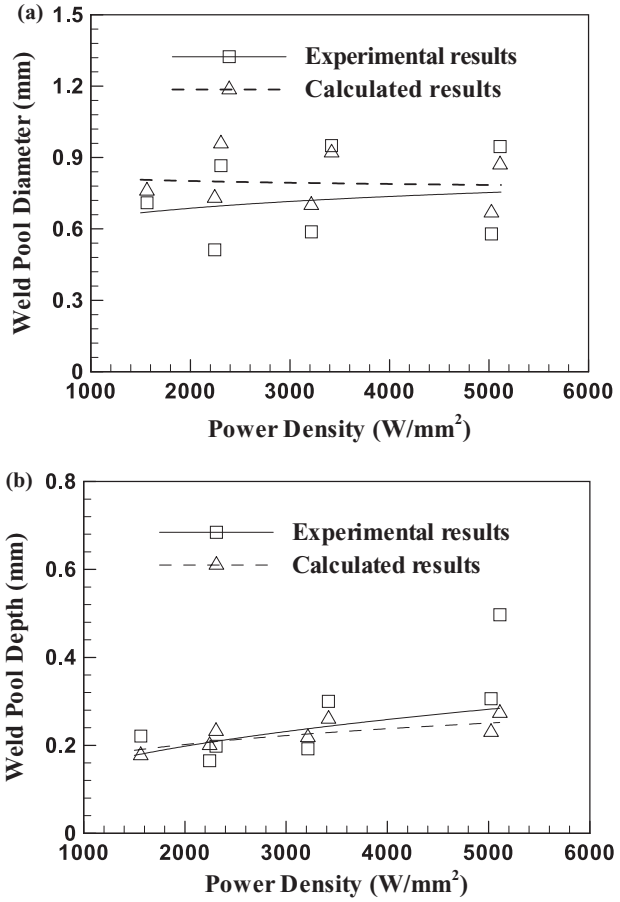

Figure 2. The experimental and calculated results of effects of laser power density on (*a*) the weld pool diameter and (*b*) the weld pool depth. The power density is defined as the ratio of power and the laser beam area of cross section.

velocities increase with time. At the end of the pulse, the peak temperature drops and the weld pool shrinks rapidly, as shown in figures 3(*d*) and (*e*). The liquid flow during heating is mainly driven by surface tension force and to a much less extent by the buoyancy force. This matter will be discussed more fully using dimensionless numbers. The calculations

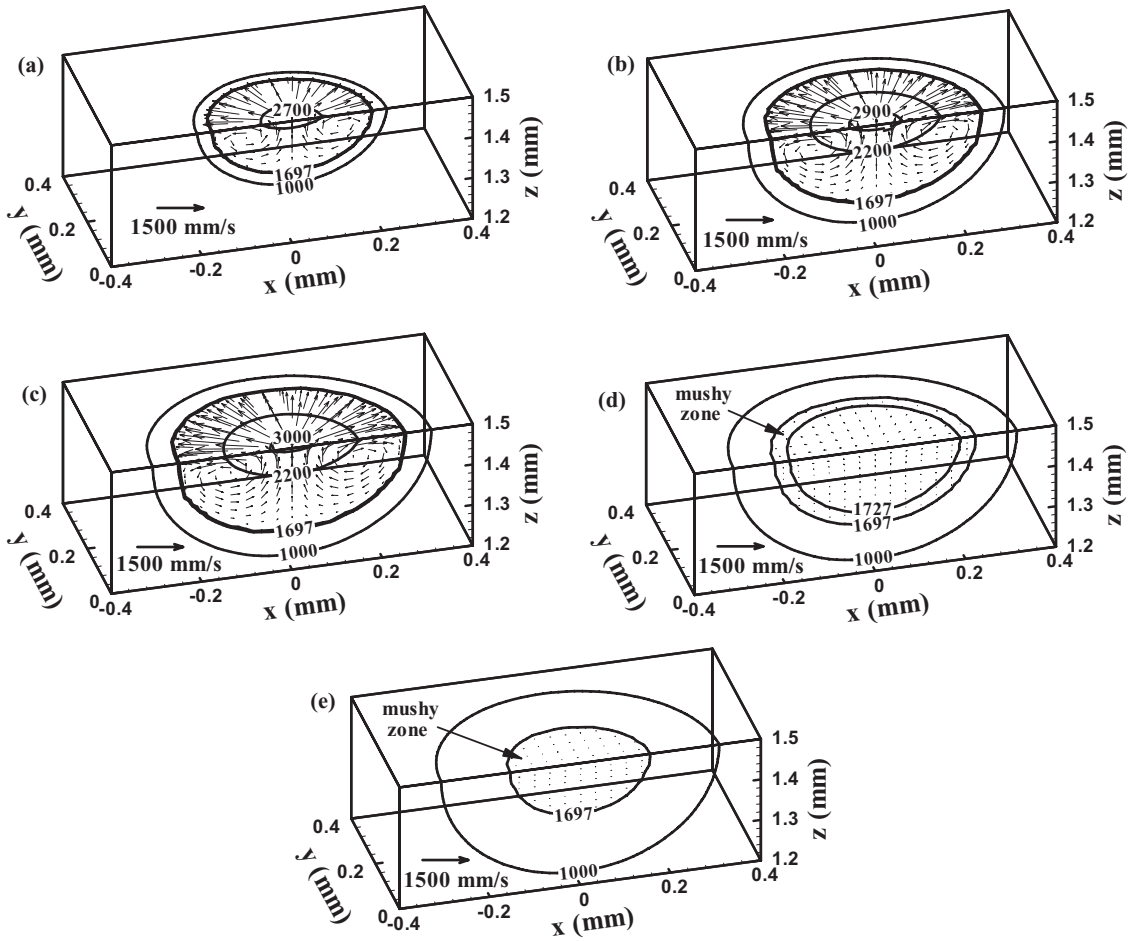

Figure 3. Computed temperature and velocity fields at different times: (*a*) $t = 1$ ms, (*b*) $t = 3$ ms, (*c*) $t = 4$ ms, (*d*) $t = 4.5$ ms and (*e*) $t = 5$ ms. Laser power: 530 W, pulse duration: 4.0 ms, and beam radius: 0.159 mm.

show that the weld pool solidifies completely in about 1.7 ms after the laser pulse is switched off. The maximum velocity in the weld pool is about 95 cm s^{-1}, while at the time of 5.0 ms (1.0 ms after the laser is switched off), the maximum velocity is still about 0.4 cm s^{-1} driven mainly by inertia.

A two-phase solid–liquid mushy zone exists in the thin region between the solidus (1697 K) and liquidus (1727 K) isotherms. The size of this zone is very small during heating as shown in figures 3(*a*)–(*c*). At the end of the pulse, the size of the mushy zone increases significantly as can be observed from figures 3(*d*) and (*e*). The evolution of mushy zone during laser spot welding is discussed in detail in a later section.

4.3. Weld thermal cycle

Figure 4 shows the changes in the computed temperatures at various monitoring locations. The monitoring locations 2, 3 and 4 are at 0.1 mm distance from the weld centre but at 0°, 45°, and 90° planes, respectively. Similarly, monitoring locations 5, 6 and 7 are at 0.2 mm from the weld centre along 0°, 45°, and 90° planes, respectively. The results indicate that initially the heating rate in the weld pool is very fast. With the increase in temperature, the heating rate decreases gradually until the laser is switched off. When the solidification starts, the temperature decreases quickly until it is close to the liquidus temperature. At this temperature, there is a plateau in the thermal cycle curves indicating very low cooling rate due to the release of the latent heat of fusion, as discussed in the next section. When the weld pool cools below the liquidus temperature, the temperature decreases gradually.

The peak temperatures and the heating rates vary significantly depending on the location. Similarly, the cooling rates above the liquidus temperature vary significantly. However, as the weld metal cools, the spatial variation of the cooling rates decreases. When the temperature drops below the solidus temperature, the variation of the cooling rate becomes small due to nearly constant outward heat loss from all locations of the weld. Thus, the spatial variation of the microstructure is expected to be small in the weld metal, except in certain special steels whose microstructures are highly sensitive to cooling rate.

From figure 4, it can also be seen that the thermal cycles at locations equidistant from the weld centre show considerable variation. At the top surface, i.e. x–y plane, the shape of the weld pool is close to a circle. As a result, the temperatures at different locations equidistant to the weld centre are the same. However, in the x–z plane, the temperatures at the 0° plane, represented by curve 2 are higher than those at the 90° plane represented by curve 4 although both locations are at a distance of 0.1 mm from the location of the laser beam axis. This variation is mainly due to the shallow pool geometry which increases the temperature gradient along the 90° plane in

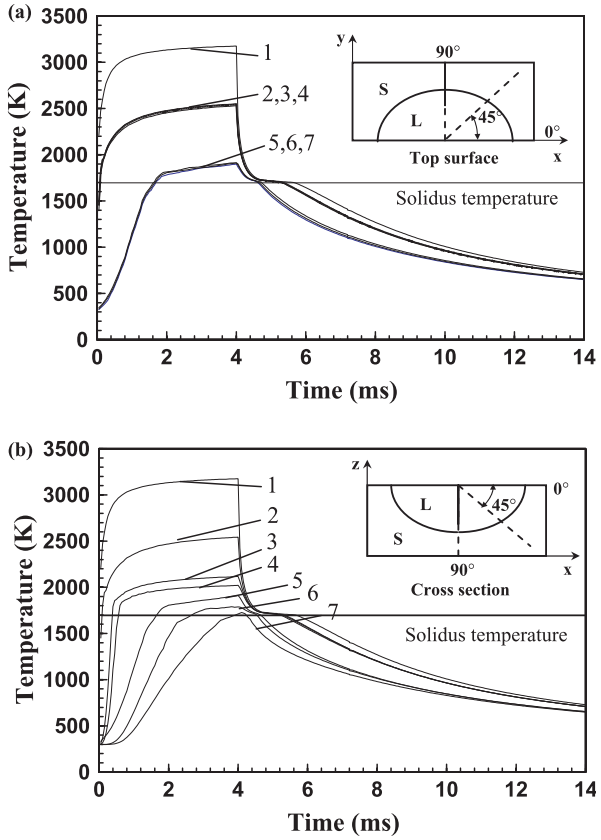

Figure 4. Weld thermal cycles at different locations. (*a*) Top surface; (*b*) cross section. Distance from the weld centre: 1: 0.0 mm; 2: 0.1 mm at 0°; 3: 0.1 mm at 45°; 4: 0.1 mm at 90°; 5: 0.2 mm at 0°; 6: 0.2 mm at 45°; and 7: 0.2 mm at 90°, as shown in the small figure. Calculated weld pool radius is 0.254 mm and the depth is 0.202 mm. So all points are in the weld pool at some time. The solid horizontal lines indicates solidus temperature. Laser power: 530 W, pulse duration: 4.0 ms, and beam radius: 0.159 mm.

comparison with the 0° plane. The average temperature gradient in the weld pool at the 90° location is higher than that at the 0° plane since the weld pool is shallow and wide. For locations at the same distance to the weld centre, the higher the average temperature gradient, the lower the temperature. Therefore, at locations equidistant from the weld centre, the temperatures at the 0° plane are the highest and those at the 90° plane are the lowest. A similar observation was also made by Wei *et al* [33] while studying GTA spot welding.

4.4. Role of convection from dimensionless numbers

4.4.1. Relative importance of heat transfer by conduction and convection. In the weld pool, heat is transported by a combination of convection and conduction. The relative importance of convection and conduction in the overall transport of heat can be evaluated from the value of Peclet number, *Pe*, which is defined by

$$Pe = \frac{u\rho C_p L_R}{k} \tag{14}$$

where u is the average velocity, L_R is the characteristic length taken as the pool radius at the top surface of weld pool, ρ, C_p and k have been defined earlier. When *Pe* is less than 1, the heat

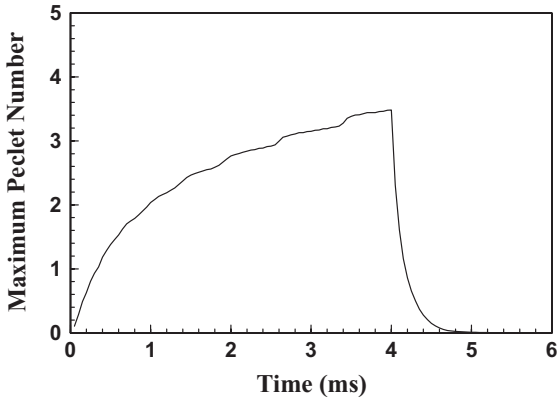

Figure 5. The variation of maximum Peclet number with time. Laser power: 530 W, pulse duration: 4.0 ms, and beam radius: 0.159 mm.

transport within the weld pool occurs primarily by conduction. When *Pe* is much higher than 1, the primary mechanism of heat transfer is convection. For spot welding, the value of Peclet number is a function of time since both u and L_R depend on time. Figure 5 shows the change of maximum Peclet number with time in the weld pool. It can be seen that at the beginning of pulse cycle, the Peclet number is low and conduction is the primary mechanism of heat transfer. With time, the Peclet number increases and convection becomes more important heat transport mechanism in the weld pool. When the pulse is switched off, the Peclet number drops to a very low value very quickly and conduction becomes the main mechanism of heat transfer again due to rapid decrease in velocity.

4.4.2. Relative importance of different driving forces. Several dimensionless numbers have been used in the literature to determine the relative importance of different driving forces in the weld pool [37]. The ratio of buoyancy force to viscous force is determined by Grashof number:

$$Gr = \frac{g\beta L_b^3 \Delta T \rho^2}{\mu^2} \tag{15}$$

where g is the gravitational acceleration, β is the thermal expansion coefficient, ΔT is the temperature difference between the peak pool temperature and solidus temperature and L_b is a characteristic length for the buoyancy force in the liquid pool which is approximated by one eighth of the pool radius [37]. Surface tension Reynolds number, *Ma*, is used to describe the ratio of surface tension gradient force to viscous force, and is calculated as:

$$Ma = \frac{\rho L_R \Delta T |\partial\gamma/\partial T|}{\mu^2} \tag{16}$$

Using the physical properties listed in table 2 and the experimental conditions of figure 3, *Gr* and *Ma* at $t = 4$ ms (i.e. just before the laser is switched off) are calculated as follows:

$$Gr = \frac{980 \times 1.96 \times 10^{-5}(0.0256 \times (1/4))^3 \times 1400 \times 7.2^2}{1^2} = 3.65 \times 10^{-4} \tag{17}$$

$$Ma = \frac{7.2 \times 0.0256 \times 1400 \times 0.43}{1^2} = 110.96 \tag{18}$$

The relative importance of the primary driving forces can be judged by the combination of these dimensionless numbers. The ratio of surface tension force to buoyancy force is expressed as:

$$R_{s/b} = \frac{Ma}{Gr} = \frac{110.96}{3.65 \times 10^{-4}} = 3.04 \times 10^5 \qquad (19)$$

Therefore, it can be expected that the liquid flow is mainly driven by Marangoni convection and to a much less extent by the buoyancy force.

4.4.3. Order of magnitude of maximum velocity in the weld pool. Since the surface tension force is the dominant driving force for convection in the weld pool, the order of the maximal velocity can be approximated by [38]:

$$u_m^{3/2} \approx \frac{d\gamma}{dT}\frac{dT}{dy}\frac{W^{1/2}}{0.664\rho^{1/2}\mu^{1/2}} \qquad (20)$$

where dT/dy is the average temperature gradient in the weld pool, W is the weld pool radius and the other variables have been defined before. Substituting corresponding value, we can get

$$u_m \approx \left(0.43 \times 0.2 \times 10^5 \times \frac{0.0256^{1/2}}{0.664 \times 7.2^{1/2} \times 1^{1/2}}\right)^{2/3} = 84.1\ \mathrm{cm\,s^{-1}} \qquad (21)$$

This value is in good agreement with that calculated using the three-dimensional transient heat transfer and fluid flow model, where the maximum velocity at $t = 4$ ms was found to be about 95 cm s^{-1}.

The foregoing dimensional analysis provided insights about the weld pool development during spot welding. It should be noted that these order of magnitude analyses cannot provide accurate and detailed information about the spot welding processes, which requires numerical calculation with very fine grids and small time steps.

4.5. Evolution of mushy zone

The Evolution of mushy zone size during the laser spot welding is shown in figure 6. During heating, the liquidus and solidus isotherms are very close and the resulting size of mushy zone is very small. After the pulse is switched off, the mushy zone expands initially and the maximum size of the mushy zone is reached when the pure liquid region diminishes. The size of the mushy zone then decreases as solidification proceeds further.

The initial expansion of the mushy zone size could be explained by considering the effect of the latent heat of fusion. When the temperature is higher than the liquidus temperature, the heat loss is accompanied by a decrease in temperature. As the temperature drops between the liquidus and solidus temperatures, the heat loss comes mainly from the release of the latent heat of fusion and the temperature decrease is very slow. As a result, the liquidus isotherm moves faster than the solidus isotherm until the pure liquid region vanishes and the entire weld pool is transformed to mushy region. The evolution of the mushy zone during solidification is demonstrated more clearly in figure 7. As shown in this figure, the pure liquid region disappears in about 0.8 ms after the solidification starts and the mushy zone exists for about another 0.9 ms before the weld pool solidifies completely. The existence of a large mushy region is a unique feature of the solidification during spot welding [7, 33].

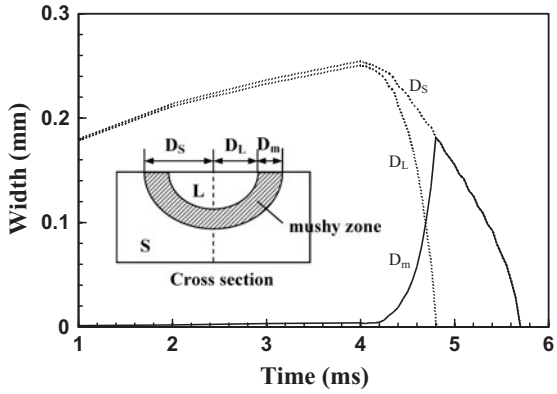

Figure 6. Evolution of the mushy zone size during laser spot welding. The symbols D_L and D_S are the distances from the weld centre to the liquid/mushy zone and mushy zone/solid interfaces at the pool top surface, respectively. The size of the mushy zone, D_m, is defined as the difference between D_L and D_S, as shown in the small figure. Laser power: 530 W, pulse duration: 4.0 ms, and beam radius: 0.159 mm.

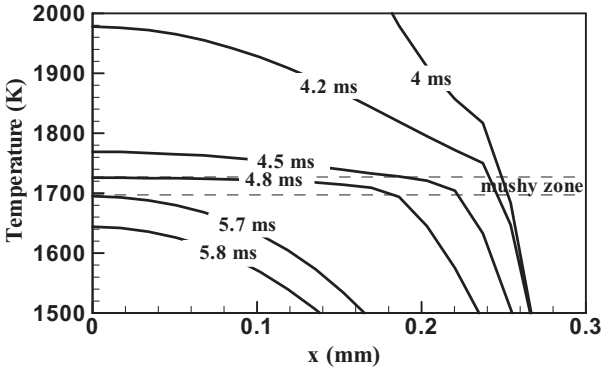

Figure 7. Distribution of temperature at the pool top surface at various solidification times. Time equal to 4 ms corresponds to the time when solidification starts. Laser power: 530 W, pulse duration: 4.0 ms, and beam radius: 0.159 mm.

4.6. Solidification

During the rapid solidification of the weld pool, the critical parameters in determining the fusion zone microstructure are temperature gradient (G), solidification growth rate (R), undercooling (ΔT) and alloy composition. Undercooling, ΔT, indicates how far a liquid alloy of given composition is cooled below its equilibrium liquidus temperature. Since weld solidification proceeds from the preexisting solid substrate, only undercooling associated with growth is important. The undercooling is comprised of contributions from thermal, constitutional, kinetic and solid curvature effects [38]. In this study, in order to simplify the calculations, no undercooling is considered. The solidification parameters were calculated by considering only the heat transfer and fluid flow in the weld pool. In other words, the equilibrium liquidus isotherm is

assumed to represent the liquid/mushy zone boundary, while the equilibrium solidus isotherm was assumed to be the mushy zone/solid boundary.

Figure 8 shows distances of the mushy zone/liquid interface to the weld centre as a function of time for two laser power densities (cases A and B). The symbols, D_0 and D_{90} represent the distances between the mushy zone/liquid front and the weld centre at 0° and 90° planes. It is observed that for case A, D_0 and D_{90} are very close to each other, while for case B, D_0 is twice that of D_{90} due to the use of larger beam radius. From this figure, the solidification rate, defined as the rate at which the mushy zone/liquid interface in the weld pool advances, can be calculated as the slopes of distance versus time. Figures 9 and 10 show the four important parameters of solidification, temperature gradient (G), solidification rate (R) and their combinations GR and G/R as a function of the time at the 0° and 90° planes for cases A and B, respectively. The temperature gradients, G_0 and G_{90}, are evaluated in the liquid at the mushy zone/liquid interface. The figures show that G_0 and G_{90} at both planes decrease with time, while the solidification rates at both planes increase with time. The maximum solidification rate is reached when the weld pool solidifies completely. In order to understand the solidification phenomena, let us consider the following heat balance equation [33]:

$$R = \frac{\mathrm{d}r}{\mathrm{d}t} = \frac{k_S G_S - k_L G_L}{\bar{f_L} L} \tag{22}$$

where G_S and G_L are the temperature gradient in liquid at the mushy zone/liquid interface, respectively, k_S and k_L are the thermal conductivities in the solid and the liquid, respectively, and f_L is the liquid fraction. As shown in figure 7, G_L drops more rapidly than G_S during solidification. Furthermore, f_L decreases with time as the solidification progressed. As a result, the solidification rate increases with time, which is indicated in figures 9(b) and 10(b).

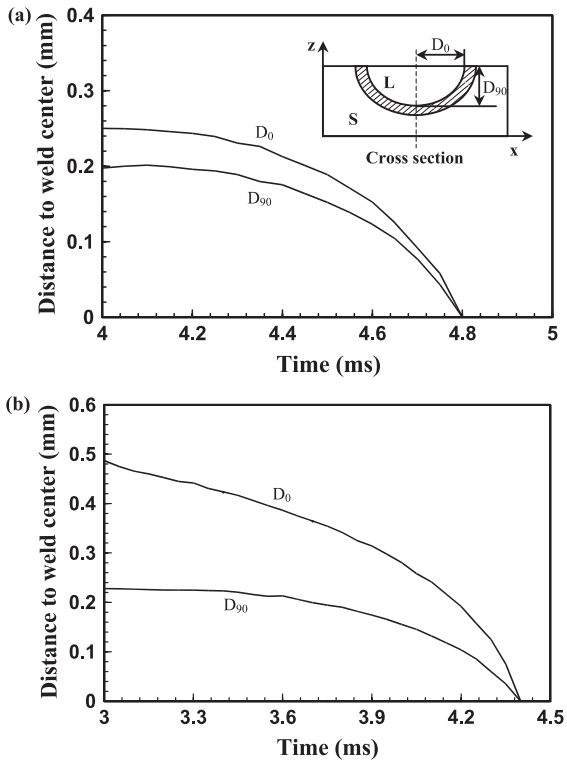

Figure 8. Distance between the mushy zone/liquid front and weld centre as a function of time. (*a*) Laser power: 530 W, pulse duration: 4.0 ms, and beam radius: 0.159 mm. (*b*) Laser power: 1967 W, pulse duration: 3.0 ms, and beam radius: 0.57 mm.

The solidification rate, R, and temperature gradient, G, are important in the combined forms G/R and GR (cooling rate). As shown in figures 9(c) and 10(c), the solidification parameter G/R decreases with time, since G decreases while R increases with time. The solid–liquid interface stability factor, G/R, is related to the solidification morphology. As the value of G/R increases, the interface morphology changes from equiaxed-dendritic, to cellular-dendritic, to cellular grains [39]. As the solidification progresses from the mushy zone/liquid front to the weld centre, the mushy zone/liquid interface has the maximum temperature gradient and minimum solidification growth rate. While for the weld centre, the situation is completely different. It has the minimum temperature gradient and maximum solidification rate. Therefore, the value of G/R decreases from the fusion line to the weld centre. As a result, we may expect a cellular type of microstructure close to the fusion line, an equiaxed-dendritic microstructure at the pool centre, and a cellular-dendritic microstructure between these two regions.

The solidification parameter GR is useful as it influences the scale of the solidified substructure. Since G decreases and R increases with time, the value of GR does not change monotonically with time. Depending on how the rates of G and R change with time, the value of GR can either increase or decrease with time as shown in figures 9(d) and 10(d).

From figures 9 and 10, it can be seen that the solidification parameters vary with location in the weld pool. The computed values of these parameters at the mushy zone/liquid interface for 0° and 90° planes are different. These differences can be explained from weld pool geometry. From figure 8, D_0 is very close to D_{90} for case A, while for case B, D_0 is much larger than D_{90}. In other words, the weld pool cross section for case A (figure 9) is close to a hemisphere. As a result, the values of the four solidification parameters along 0° and 90° planes are very close, while for case B (figure 10), there are significant differences in the values of these four parameters between 0° and 90° planes.

It should be noted that the calculated solidification parameters have not been validated by comparing with the corresponding experimental results in 304 stainless steel laser spot welds. Calculations presented here indicate aspects of solidification in a qualitative manner, since the focus here was the examination of the results of the transient heat transfer and fluid flow model. Furthermore, the solidification process investigated in this model is governed only by the transfer of heat. An accurate prediction of the weld pool solidification will require consideration of both the thermodynamics and kinetics of solidification.

4.7. Comparison of laser spot welding with GTA spot welding and GTA linear welding

Laser spot welding is characterized by a much shorter time span than the GTA spot welding or GTA linear welding. As

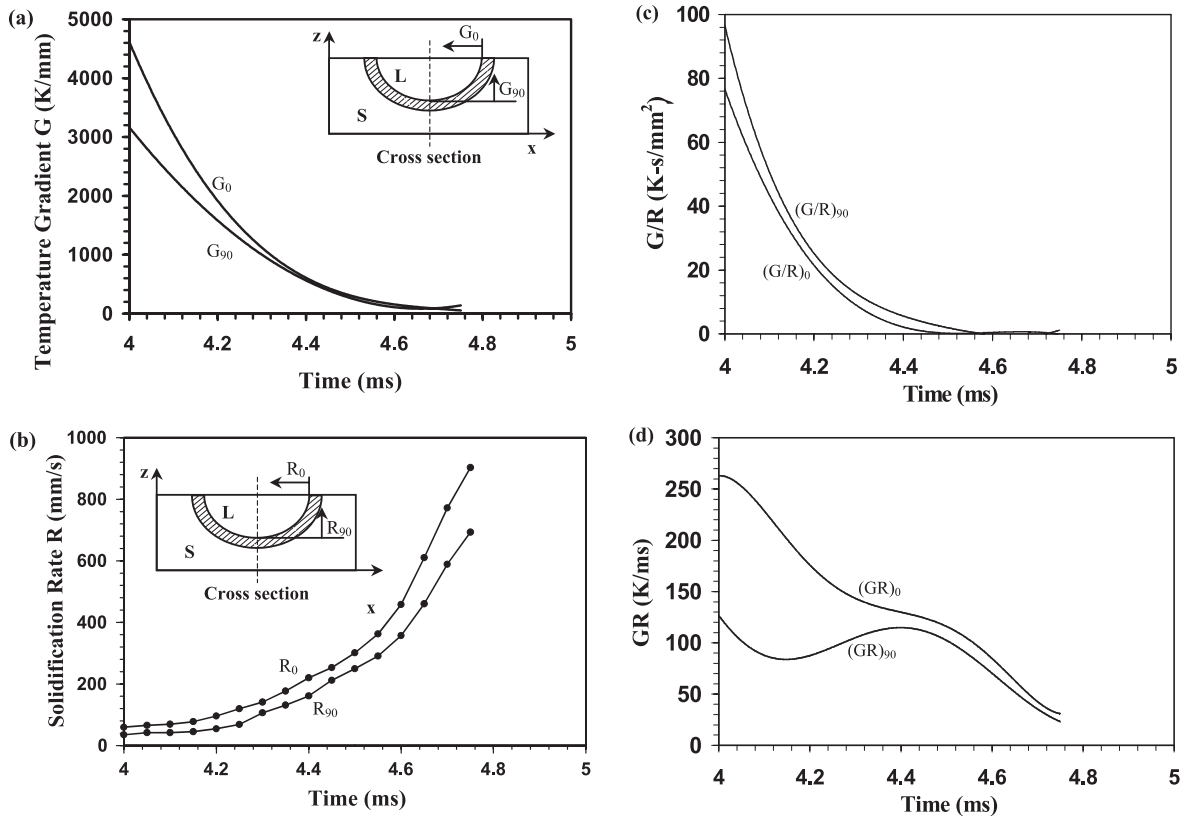

Figure 9. The values of G, R, G/R, GR along 0° and 90° planes at the mushy zone/liquid interface as a function of time. (*a*) G; (*b*) R; (*c*) G/R; (*d*) GR. Laser power: 530 W, pulse duration: 4.0 ms, and beam radius: 0.159 mm.

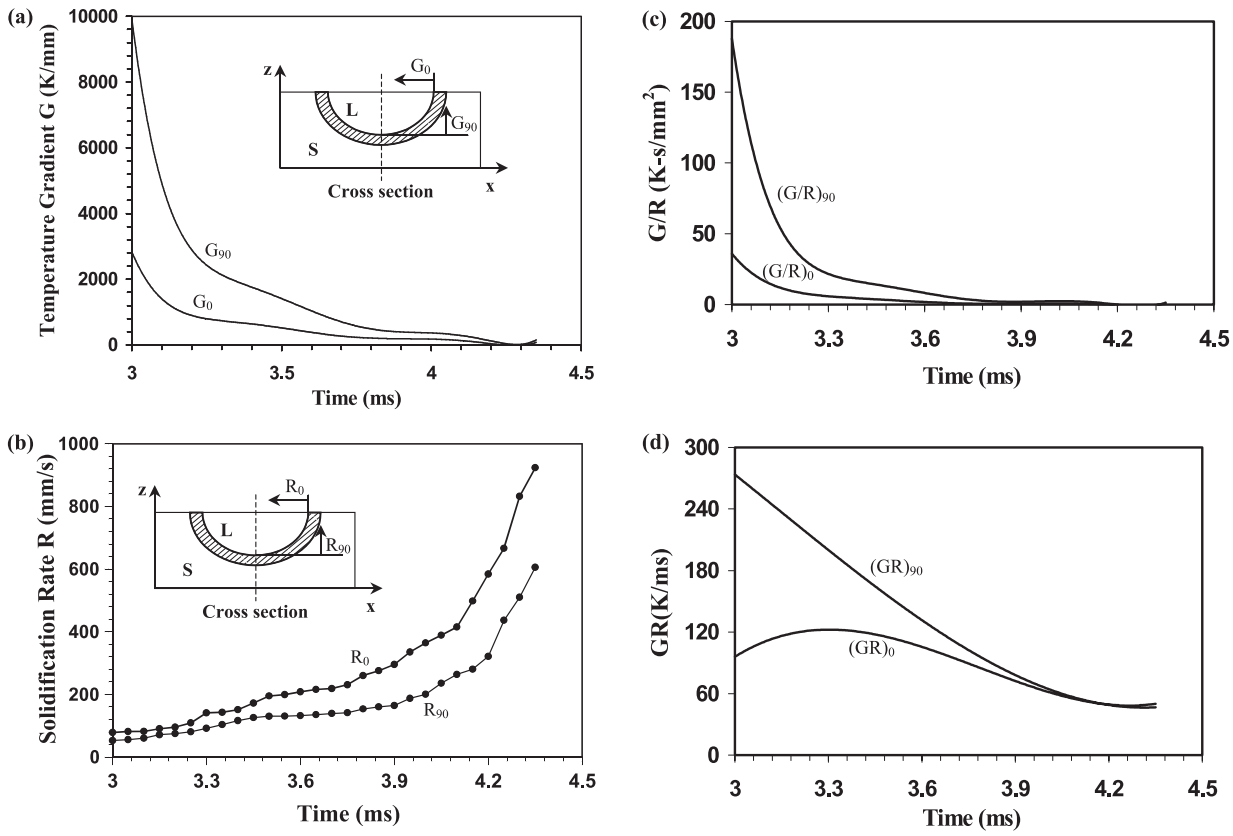

Figure 10. The values of G, R, G/R, GR along 0° and 90° planes at the mushy zone/liquid interface as a function of time. (*a*) G; (*b*) R; (*c*) G/R; (*d*) GR. Laser power: 1967 W, pulse duration: 3.0 ms, and beam radius: 0.57 mm.

a result, the temperature gradients in the work piece and its cooling rates are significantly different in the three processes. The computed values of spatial and the temporal variations of temperature for the three welding processes are compared in table 3. The laser spot welding is characterized by higher power intensity, higher peak temperature and smaller weld pool size. As a result, the cooling rate, temperature gradient and the solidification rate in the weld pool are much higher than those in GTA linear and spot welding. The computed results in table 3 indicate that during laser spot welding, the maximum temperature gradient in the weld pool can reach to 3050 K mm^{-1} and the maximum solidification rate can be as high as 920 mm s^{-1}. For a typical GTA spot welding of 1005 steel, the maximum temperature gradient in the weld pool is about 430 K mm^{-1} and solidification rate of 30 mm s^{-1}. More important, the cooling rate in the laser spot welding is significantly higher than the GTA welding. Therefore, it is possible to obtain the different solidification substructures in the fusion zone depending on the welding process. The computed results in the table provide a good understanding of the relative values of important parameters for the three welding processes. However, the results must be used with caution, since the temperature gradients and the cooling rates presented in table 3 depend strongly on the welding parameters.

5. Conclusions

(1) The fusion zone geometry, calculated from the transient heat transfer and fluid flow model, was in good agreement with the corresponding experimentally measured values for various laser spot welding conditions. During heating, the heating rate varies significantly at different locations. As the weld pool cools below the solidus temperature, the spatial variation of cooling rates decreases.

(2) The liquid flow is mainly driven by the surface tension and to a much less extent, by the buoyancy force. Liquid metal convection significantly affects heat transfer in the weld pool towards the end of the pulse. Heat transfer by conduction is important when the liquid velocity is small at the beginning of the pulse and during weld pool solidification.

(3) The size of the mushy zone, i.e. liquid + solid two-phase region, grows significantly with time during solidification and the maximum size of the mushy zone is reached when the pure liquid region vanishes. This behaviour can be explained from the heat transfer consideration taking into account the latent heat of fusion.

(4) The temperature gradients (G) in the liquid at the mushy zone/liquid interface decrease with the solidification time. The solidification rate (R) of the mushy zone/liquid interface increases with time. The combination of solidification parameters G and R, i.e. G/R and GR, were quantitatively calculated in laser spot welding of 304 stainless steel.

(5) For laser spot welding, the cooling rate, temperature gradient and the solidification rate in the weld pool were much larger than those for GTA linear welding and GTA spot welding.

Table 3. Comparison of laser spot welding variables with GTA linear welding [18] and GTA spot welding [33].

	GTA linear welding	GTA spot welding	Laser spot welding
Materials	AISI 1005 carbon manganese steel	AISI 1005 carbon manganese steel	304 stainless steel
Power (kW)	1.9	1.9	1.9
Beam radius (mm)	2.35	2.35	0.57
Pulse duration/ welding velocity	Velocity = 0.6 mm s^{-1}	16 s	3 ms
Peak temperature (K)	2000	2100	2700
Depth (mm)	1.85	1.8	0.22
Half-width (mm)	4.41	4.3	0.48
Cooling rate between 773 and 1073 K (K s^{-1})	40	250	41 380
Maximum temperature gradient at the top surface (K mm^{-1})	120	430	3050
Maximum solidification rate at the top surface (mm s^{-1})	0.6	30	920

Acknowledgments

The work was supported by a grant from the US Department of Energy, Office of Basic Energy Sciences, Division of Materials Sciences, under grant number DE-FGO2-01ER45900. The experimental work was performed at Sandia National Laboratories, which is supported by the US Department of Energy under contract number DE-AC04-94AL85000. The authors thank Mr Wei Zhang, Mr Saurabh Mishra, Mr Yajun Fan, Mr Amit Kumar, Dr Cheolhee Kim and Dr Amitava De for their comments on various drafts of this paper.

References

[1] Cline H E and Anthony T R 1977 *J. Appl. Phys.* **48** 3895
[2] Mazumder J and Steen W M 1980 *J. Appl. Phys.* **51** 941
[3] Frewin M R and Scott D A 1999 *Weld. J.* **78** 15s
[4] Katayama S, Mizutani M and Matsunawa A 1997 *Sci. Technol. Weld. Joining* **2** 1
[5] Chang W S and Na S J 2001 *Metall. Trans.* B **32B** 723
[6] Oreper G M, Szekely J and Eager T W 1986 *Metall. Trans.* B **17B** 735
[7] Betram L A 1993 *J. Eng. Mater. Technol.* **115** 24
[8] Sahoo P, Collur M M and DebRoy T 1988 *Metall. Trans.* B **19B** 967
[9] Paul A and DebRoy T 1988 *Metall. Trans.* B **19B** 851
[10] Khan P A A and DebRoy T 1984 *Metall. Trans.* B **15B** 641
[11] Collar A M M, Paul A and DebRoy T 1987 *Metall. Trans.* B **18B** 733
[12] Zacharia T, David S A, Vitek J M and DebRoy T 1989 *Weld. J.* **68** 499s
[13] Mundra K and DebRoy T 1993 *Metall. Trans.* B **24B** 145
[14] Hong T, DebRoy T, Babu S S and David S A 2000 *Metall. Trans.* B **31B** 161
[15] Mundra K, DebRoy T, Babu S S and David S A 1997 *Weld. J.* **76** 163s

[16] Zhao H and DebRoy T 2001 *Metall. Trans.* B **32B** 163
[17] Yang Z, Sista S, Elmer J W and DebRoy T 2000 *Acta Mater.* **48** 4813
[18] Zhang W, Elmer J W and DebRoy T 2002 *Mater. Sci. Eng.* A **333** 320
[19] Mundra K, Blackburn J M and DebRoy T 1997 *Sci. Technol. Weld. Joining* **2** 174
[20] Palmer T A and DebRoy T 2000 *Metall. Trans.* B **31B** 1371
[21] Fuerschbach P W and Norris J T 2002 *Beam Characterization for Nd : YAG Spot Welding Lasers* Presented at *ICALEO 2002 (Scottsdale, AZ)*
[22] Zacharia T, David S A, Vitek J M and DebRoy T 1989 *Weld. J.* **68** 510s
[23] Patankar S V 1980 *Numerical Heat Transfer and Fluid Flow* (New York: Hemisphere Publishing Corporation)
[24] Voller V R and Prakash C 1987 *Int. J. Heat Mass Transfer* **30** 1709
[25] Brent A D, Voller V R and Reid K J 1988 *Numer. Heat Transfer* **13** 297
[26] Tsai N S and Eagar T W 1985 *Metall. Trans.* B **16B** 841
[27] Chan C L, Zehr R, Mazumder J and Chen M M 1986 *Modelling and Control of Casting and Welding Processes* ed S Kou and R Mehrabian, p 229
[28] Cremers D A, Lewis G K and Korzekwa D R 1991 *Weld. J.* **70** 159s
[29] Pitscheneder W 2001 *PhD Thesis* The University of Leoben
[30] Ready J F 2001 *LIA Handbook of Laser Materials Processing* (Orlando: Magnolia Publishing)
[31] Bramson M A 1968 *Infrared Radiation: A Handbook for Applications* (New York: Plenum)
[32] Peckner D and Bernstein I M 1977 *Handbook of Stainless Steels* (New York: McGraw-Hill)
[33] Zhang W, Roy G G, Elmer J W and DebRoy T 2003 *J. Appl. Phys.* **93** 3022
[34] Davis J R 1998 *Metals Handbook* (Materials Park, OH: ASM International)
[35] Davis J R 1994 *ASM Specialty Handbook. Stainless Steel* (Materials Park, OH: ASM International)
[36] ASM International Handbook Committee 1990 *Metals Handbook. Vol 1. Properties and Selection: Iron, Steels, and High-performance Alloys* (Materials Park, OH: ASM International)
[37] Yang Z 2000 *PhD Thesis* The Pennsylvania State University
[38] DebRoy T and David S A 1995 *Rev. Mod. Phys.* **67** 85
[39] Grong Ø 1997 *Metallurgical Modeling of Welding* 2nd edn (London: The Institute of Materials)